Single crystalline $BaTiO_3$ thin films synthesized using ion implantation induced layer transfer

Young-Bae Park, Kenneth Diest,[a] and Harry A. Atwater
Thomas J. Watson Laboratory of Applied Physics, California Institute of Technology, Pasadena, California 91125

(Received 8 May 2007; accepted 14 August 2007; published online 11 October 2007)

Layer transfer of $BaTiO_3$ thin films onto silicon-based substrates has been investigated. Hydrogen and helium ions were co-implanted to facilitate ion-implantation-induced layer transfer of films from $BaTiO_3$ single crystals. From thermodynamic equilibrium calculations, we suggest that the dominant species during cavity nucleation and growth are H_2, H^+, H_2O, Ba^{2+} and Ba–OH, and that the addition of hydrogen to the Ba–Ti–O system can effectively suppress volatile oxide formation during layer transfer and subsequent annealing. After ion implantation, $BaTiO_3$ layers contain microstructural defects and hydrogen precipitates in the lattice, but after layer transfer, the single crystal is found to be stoichiometric. Using direct wafer bonding and layer splitting, single crystal $BaTiO_3$ thin films were transferred onto amorphous Si_3N_4 and Pt substrates. Micro-Raman spectroscopy indicated that the density of defects generated by ion implantation in $BaTiO_3$ can be significantly reduced during post-transfer annealing, returning the transferred layer to its single crystal state. Characterization using piezoresponse force microscopy shows that the layer transferred thin films are ferroelectric, with domain structures and piezoresponse characteristics similar to that of bulk crystals. © *2007 American Institute of Physics*. [DOI: 10.1063/1.2786915]

I. INTRODUCTION

Ferroelectric materials have attracted increased attention as device materials in recent years because of their potential applications in microelectronics and integrated optics.[1] Furthermore, these materials are attractive for microelectromechanical systems (MEMS) applications due to large displacement and high output force during actuation.[2]

Many different methods have been studied to obtain high-quality, thin film ferroelectric layers.[3] The growth of epitaxial thin films at relatively high temperatures (>700 °C) has been reported using metal organic chemical vapor deposition, molecular beam epitaxy, atomic layer deposition, pulsed laser deposition, chemical solution deposition, and sol-gel processes. Integration of most of these technologies with conventional silicon-based device applications has proven difficult because of the high growth temperatures required and the need for an epitaxial template. Due to the complex set of elastic and electric boundary conditions at each grain, the grains in pressed ceramics and polycrystalline films are usually composed of multiple domains. If the spontaneous polarization within each domain is random, or distributed in such a way as to lead to zero net polarization, the pyroelectric and piezoelectric effects of individual domains will partially or significantly compensate each other. Additionally, for photonic devices, grain boundaries and domain boundaries can be sources of light scattering and absorption.

Recently, progress on integration of single crystal ferroelectrics has been made by fabrication of single crystal thin film layers. Light elements such as hydrogen and helium are implanted into a wafer at a specified projected range, and a film of equivalent thickness is exfoliated.[4,5] Recently, successful layer transfer of semiconductors and ferroelectric materials has been reported.[6–12] In that work, transferred layers were fabricated and bonded using organic elastomers, and the layer transfer was accomplished by formation of a sacrificial layer which was later chemically etched away. In the work reported here, layer transfer relies on direct wafer bonding and gas pressure-induced layer exfoliation. This is similar to that used to fabricate silicon-on-insulator structures, and enables much thinner films to be fabricated. We discuss hydrogen release and the resulting cavity growth mechanisms for the layer splitting of $BaTiO_3$, and the role of hydrogen during post-thermal annealing. Together with the thermodynamics and kinetics of cavity nucleation, growth, and blistering, these results provide an explanation of the layer exfoliation process. In this study, H^+ and He^+ were implanted in single crystal $BaTiO_3$ and subsequently bonded to Si_3N_4/Si and Pt/Si receptor substrates, which are typical structures for ferroelectric memory and MEMS devices. Pt is typically used as a bottom electrode in ferroelectric capacitors and Si_3N_4 is typically used as an etch-stop layer in MEMS devices.

II. EXPERIMENT

Protons were implanted into single crystal $BaTiO_3$ with energy between 20 and 80 keV with a dose of 5×10^{16}–1×10^{17} cm^{-2}, followed by 30–115 keV He^+ implantation with a dose of 1×10^{17} cm^{-2}. All implantations were performed at room temperature. The donor and receptor substrates (sputtered Pt on Si and low pressure chemical vapor deposition Si_3N_4 on Si) were cleaned with methanol, acetone, and de-ionized water. The donor and receptor substrates were bonded by hand at room temperature. Heating

[a]Electronic mail: diest@caltech.edu

during the initial bonding step causes micocracks to form and cavities to nucleate, coalesce, and blister in the implanted region. Isochronal annealing of the bonded donor material was performed between 300 and 500 °C after initial bond formation, causing a layer whose thickness is equal to the implanted depth to be transferred to the receptor substrate.

The thermodynamic equilibrium composition at the annealing temperature (300–700 °C) was calculated using the SOLGASMIX-PV code in Chemsage,[13] minimizing the total Gibbs free energy of the system with data from the JANAF thermochemical table.[14] Calculations were performed for both Ba–Ti–O and Ba–Ti–O–H systems with the compound conditions of 1:1:3 and 1:1:3:0.1-10, respectively, corresponding to stoichiometric single crystal $BaTiO_3$ with and without the addition of hydrogen.

Blistering was observed by polarized optical microscopy, scanning electron microscopy, and atomic force microscopy. Atomic force microscopy was also used to characterize transferred film thickness and surface roughness. Micro-Raman spectroscopy, Rutherford backscattering spectroscopy, forward recoil elastic spectroscopy, energy dispersive x-ray spectroscopy, and transmission electron microscopy analyses were performed to assess the microstructural evaluation of the bulk crystal and transferred layer. Ferroelectric domain imaging and microscopic hysteresis loop measurements were obtained using piezoresponse force microscopy.

III. RESULTS AND DISCUSSION

A. Donor and receptor substrate characteristics

The key factors required to achieve covalent bonding between donor and receptor substrates are high surface flatness, low surface roughness, surface cleanliness, and chemical reactivity. Initial bonding of bulk, unimplanted $BaTiO_3$ crystals was successful since the donor and receptor substrates can be prepared according to these conditions. Bulk (100) $BaTiO_3$ has a typical lamellar domain pattern with tetragonal 90° *a*-axis and *c*-axis domains with sizes ranging from 5 to 400 nm, with a root mean square (rms) roughness of 2.0 nm. Due to the alternating *a*-*c* tetragonal domain structure, the surface of the $BaTiO_3$ sample is corrugated with a characteristic angle between domains given by $\theta = 90° - 2\arctan(a/c)$, where a and *c* refer to lattice constants of the [100] and [001] axes, respectively. The peak-to-valley height of this surface corrugation was found to be in the range of 2–100 nm, depending on the domain size. The rms roughness of the $BaTiO_3$ donor wafer slightly increased after ion implantation to 2.4 nm. Using a Monte Carlo simulation method for calculation of ion implantation and collision cascade characteristics,[15] the ion projected range was determined to be ~430 nm.[15] The Pt coating thickness was 180 nm and the Si_3N_4 thickness was 50 nm, yielding a receptor substrate rms roughness of 0.7 nm for Si_3N_4 coated Si substrates and 3.6 nm for Pt coated Si substrates. After room temperature bonding, no interference fringes were observed, indicating a distinct lack of surface particles or other contamination. The surface energy of the $BaTiO_3$ single crystal surfaces, following H^+ implantation, was obtained by contact angle measurements using water and di-iodomethane droplets with a constant volume droplet of 20 dm^3 using a double laser-beam goniometer. At room temperature the surface energy is 61.1 mJ/m^2, and for the temperature-dependent surface energy, we used the phenomenological equation, $\gamma(T) = 6.11 \times 10^{-2} + 3.82 \times 10^{-5} T$, assuming $\gamma(T) = \gamma_o(1 + T/T_o)$, where T_o is the critical temperature at which the solid-gas interface vanishes.[15]

TABLE I. Possible equilibrium species in the Ba–Ti–O–(H) chemistry obtained from JANAF thermochemical data and SOLGASMIX-PV code.

Gas phase
H_2, H^+, H_2O, HO^-, HO_2, H_2O_2, O^{2-}, O_2, O_3
Ba^{2+}, BaH^{3+}, $BaOH^+$, Ba_2, $Ba(OH)_2$, BaO, Ba_2O,
$(BaO)_2TiO$, TiO_2, Ti^{4+}
Solid phase
$BaTiO_3$, Ba_2TiO_4, BaO, BaH_2, Ba, $Ba(OH)_2$, BaO_2TiH_2,
TiO (α), TiO (β), Ti_2O_3, TiO_2 (rutile),
TiO_2 (anatase), Ti_3O_5, Ti_4O_7, Ti, H_2O, H_2O_2

B. Hydrogen behavior in Ba–Ti–O–H phases

After ion implantation, the bulk $BaTiO_3$ lattice is filled with hydrogen. This hydrogen passivates the dangling bonds and defects generated by atomic displacements. In order to describe the behavior of hydrogen in solid materials, Sievert's law can be applied. Here $c_o = sp_e^{1/2}$ where pressure p_e is related to fugacity f_e and the hydrogen concentration c_o in the solid at equilibrium.[16] The depth profile of implanted hydrogen is determined by postimplantation diffusion as well as the as-implanted projected range profile. During annealing the hydrogen concentration profile in the solid is assumed to be in local equilibrium with hydrogen gas filled cavities. Generation of a large internal gas pressure within the cavities occurs as the material achieves local equilibrium, and thus the hydrogen concentration can be related to the input fugacity of the source hydrogen and cavity inner pressure formed during annealing.

Phase equilibrium calculations for a system composed of Ba, Ti, O, and H were performed. For constant pressure and temperature conditions, the equilibrium state is defined by a global minimum in the Gibbs free energy. We searched for the global Gibbs free energy minimum by adjusting the proportions of chemical components across all of the possible species and phases as shown in Table I, in which the 19 possible gaseous and 17 possible solid equilibrium and nonequilibrium species are shown for the Ba–Ti–O–H system. Phases that are thermodynamically unstable disappear in the search for the global Gibbs free energy minimum. We started the calculation with a fixed number of moles of Ba, Ti, O, and H, which were randomly distributed over the possible species. Phase equilibrium was defined by the values of the three independent variables that minimized the Gibbs free energy. This optimization problem was solved using SOLGASMIX-PV.[13] The independent variables were perturbed randomly to search for the global free energy minimum at fixed *P* and *T* conditions.

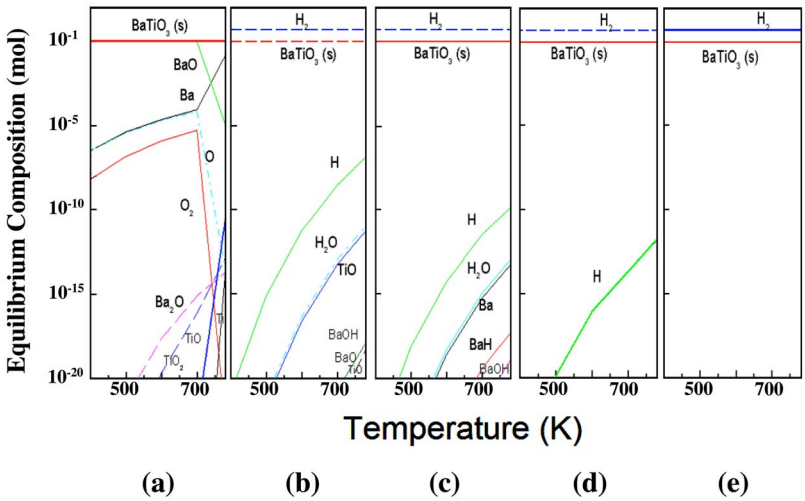

FIG. 1. (Color online) Equilibrium composition as a function of annealing temperature at the pressure of 8×10^{-4} Pa–1.33 MPa range. Equilibrium composition is obtained by using SOLGASMIX-PV code with the Ba:Ti:O=1:1:3 and Ba:Ti:O:H=1:1:3:10, assuming compound conditions at different cavity pressures. (a) 1.33×10^{-3} Pa without hydrogen, (b) 1.33×10^{-3} Pa with hydrogen, (c) 1.33×10^{3} Pa, (d) 6.7×10^{6} Pa, and (e) 13.4×10^{6} Pa.

Figure 1 shows the phase diagrams with equilibrium solid-gas species varying with respect to annealing temperature. In the absence of hydrogen, solid $BaTiO_3$ along with volatile Ti and Ba oxides are predicted as shown in Fig. 1(a). For the bulk $BaTiO_3$ material, we assumed that the bulk $BaTiO_3$ was in vacuum. On the other hand, for the system with hydrogen, we assumed that hydrogen resides at the ion projected range and forms microcavities during postimplantation processes. Figures 1(b)–1(e) clearly show a significant decrease, followed by disappearance of many of the volatile gas phase species, e.g., Ba^{2+}, Ba–O, Ba–OH, Ba–H, Ti^{4+}, and Ti–O with an increase of pressure. The calculations suggest that volatile oxide formation during high temperature annealing processes can cause the ratio of Ba^{2+} to Ti^{4+} to O^{2-} to become nonstoichiometric. However, in the presence of hydrogen, these oxide compounds can be effectively suppressed [Fig. 1(b)]. The pressurized hydrogen reduces the formation of volatile oxides and acts as an agent for cavity nucleation, growth, and blistering during the layer transfer process.

The change in concentration of gas species as a function of cavity inner pressure and geometry during annealing is shown in Fig. 2. The inner pressure is calculated based on cavity dimensions measured from atomic force microscopy and assuming that cavity nucleation occurs uniformly in all directions in the plane of ion implantation. The excess pressure in the cavity relative to ambient pressure is written as

$$\Delta p = \frac{64hEd^3}{12r^4(1-\nu^2)}, \tag{1}$$

where E is the Young modulus (120 GPa for $BaTiO_3$), d is the thickness of the layer, h is the height of the cavity, and ν is Poisson's ratio (0.3).[17] The calculated cavity pressures were between 2 and 200 MPa. The main species in this pressure range ($>10^{-9}$ mol) are H_2, H^+, H_2O, Ba^{2+}, and Ba–OH. In this range, there are no Ti-related species due to the lower free energy of formation of Ba-oxide species. In the range of pressures studied, the hydrogen gas partial pressure caused cavity nucleation followed by lateral cavity expansion. After the pressure reaches the point of cavity nucleation, the cavity begins to expand spontaneously in the rectangle area.

C. Cavity formation and real hydrogen behavior

During ion implantation, the implanted hydrogen atoms can combine with one of elements in the $BaTiO_3$ lattice forming X–H or X–OH complexes (where X is Ba or Ti) as shown by equilibrium calculations. During subsequent thermal annealing, implanted hydrogen diffuses in the vicinity of the implantation depth to form microcavities filled with H_2. The high pressure inside a cavity acts as the driving force for its growth and expansion at the initial stage of annealing.[18] The minimum implanted hydrogen dose to enable blistering can be estimated to be: $\Phi_{\min}=8\gamma/3k_BT$, where γ is a surface energy and k_B is Boltzmann's constant.[19,20] Considering the surface energy of $BaTiO_3$, one can estimate the minimum dose to be greater than 2×10^{15} ions/cm^2, which is consistent with the reported values for other ferroelectric materials.[21] The ion dose used in this study ($>1\times10^{16}$ cm^{-2}) was therefore high enough for cavity growth and blistering, Fig. 3(a).

In order to investigate hydrogen diffusion during annealing, forward recoil electron scattering spectroscopy is used. This technique measures the depth at which hydrogen and

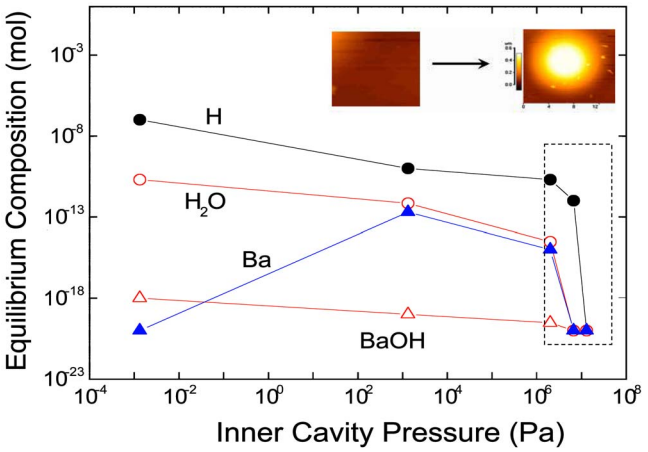

FIG. 2. (Color online) The change of pressure-dependent equilibrium composition in the Ba–Ti–O–H system at 500 °C from Fig. 1. The theoretically calculated cavity inner pressure from cavity geometry with radius and height measured by atomic force microscopy (AFM) ranges from 8×10^{-4} Pa to 0.2 GPa.

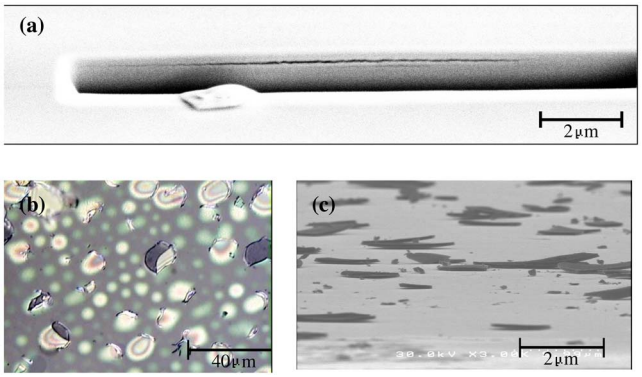

FIG. 3. (Color online) (a) Focused ion beam (FIB) image of a cavity after Ga ion etching, (b) optical microscope image of cavity distribution and blistering, and (c) SEM image of blisters on the sample surface. The average crater depth after the partial blistering is 450 nm for the lines and is consistent with the SRIM simulation results. The thickness is 450–500 nm as predicted by the SRIM simulation (1×10^{17} cm^{-2}, 80 keV).

deuterium are elastically scattered from an incident beam of energetic particles. In this case 2 MeV He^{++} was used at the Cambridge Accelerator at Harvard University Cambridge. Figure 4(a) shows the spectra for hydrogen in the implanted bulk $BaTiO_3$ after annealing at different temperatures where channel numbers 150–400 correspond to approximately 1–1.7 MeV for the energy of the recoiled particle. The behavior of hydrogen during the cavity growth and layer transfer process has been extensively studied in silicon;[22–24] however, no detailed reports on the hydrogen bonding configurations in the ferroelectric material systems have been reported. Fourier transform infrared studies in midinfrared geometries have revealed that the initial implantation damage, hydrogen passivation of internal defects and surfaces, and the physical pressure created internally by H_2 formation are all essential elements for the layer splitting and exfoliation.[25] The desorption and outdiffusion of hydrogen with partial blistering are observed in the 300–500 °C range. At 600 °C, hydrogen concentration is comparable to surface contamination level, and the overall surface of the $BaTiO_3$ was blistered, Figs. 3(b) and 3(c).

In previous work, high concentrations of hydrogen have been shown to degrade the spontaneous polarization of ferroelectrics.[26] If hydrogen bonds to one of the elements in the lattice, polar hydroxyil [OH–] bonds can form and cause asymmetric stretching motion of the O–Ti–O bond. The change of symmetry in the Ti═O bond along the polarization axis of tetragonal unit cell would degrade the spontaneous polarization and actuating properties. However, in the Ba–Ti–O–H system, thermodynamic calculations of composition show that there are no significant number of Ti–OH or Ti–H bonds, and considering the cavity inner pressure, there are no oxide species with high pressure hydrogen molecules. Also, Raman spectroscopy analysis shows no OH mode (3200–3700 cm^{-1}, not shown here).

Forward recoil electron spectroscopy was also used to investigate the hydrogen desorption kinetics. By integrating the spectroscopy measurements as a function of temperature, an Arrhenius-type reaction of hydrogen release was plotted, Fig. 4(b). By measuring the slope of this plot, the activation energy for hydrogen release was experimentally determined to be ~0.42 eV. This is similar to the corresponding energies reported for silicon.[26] It is believed that the hydrogen release reaction is not only thermally activated but also induced by physical reaction pathways generated from implantation damage. Above 600 °C, there is no considerable amount of hydrogen detected in the bulk $BaTiO_3$.

Upon thermal release of hydrogen throughout the implanted layer, the hydrogen will diffuse to form small cavities. As the pressure in these cavities increases with time, cracks begin to form, and beyond a critical radius, it will be energetically favorable for the cracks to continue growing until they merge with other cavities throughout the film. The final result is a fully exfoliated layer of $BaTiO_3$ whose thickness corresponds to the peak depth of ion implantation. This process is discussed in detail by Han and Yu.[15]

D. Microstructure of ion damaged $BaTiO_3$

In Fig. 5, micro-Raman spectroscopy shows an unprocessed, bulk $BaTiO_3$ sample with a small shoulder peak at 305 cm^{-1} and a broader peak at 710 cm^{-1}.[27] These peaks are assigned to tetragonal $BaTiO_3$ and vanish above the Curie temperature. The two broad bands centered at 272 and 513 cm^{-1} correspond to transverse optical phonons and their widths can be explained by large anharmonic coupling and a frequency dependent damping constant. The 272 and 513 cm^{-1} peaks are observed in both the cubic and tetragonal phases, although they are broader in the cubic phase. After high energy ion implantation, the bulk $BaTiO_3$ contains a damaged layer at the implantation depth. This corresponds to the low Raman active mode in the H^+ and H^+/He^+ as-implanted curves. Before the final annealing step, the broad peak at 200–400 cm^{-1}, along with the absence of a sharp 305 cm^{-1} peak and a broad 705 cm^{-1}, suggests that the

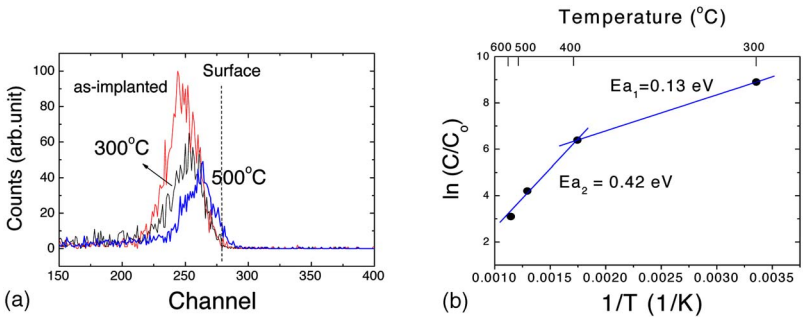

FIG. 4. (Color online) Forward recoil electron spectroscopy for (a) as-implanted $BaTiO_3$ (1×10^{17} cm^{-2}, 80 keV), annealed $BaTiO_3$ at 300 and 500 °C for 30 min. The He^+ beam (2 MeV) is incident at the angle of 150° relative to the sample surface. (b) Arrhenius-type reaction of hydrogen release from forward recoil electron spectroscopy count integration. The peak is normalized by the initial concentration (c_o) of as-implanted sample with the H^+ dose of 1×10^{17} cm^{-2} at 80 keV.

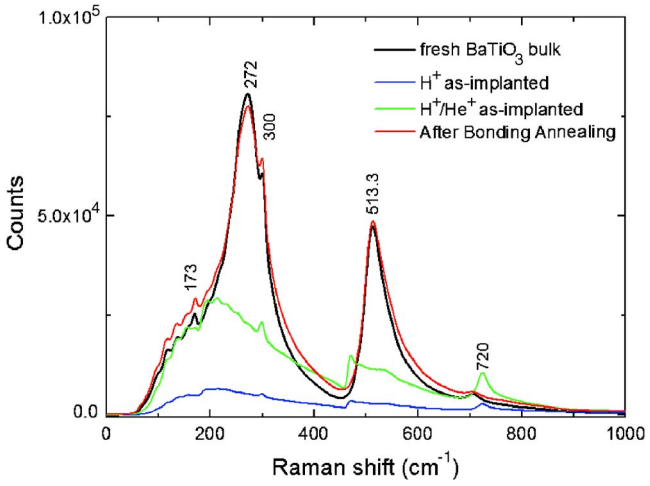

FIG. 5. (Color online) Micro-Raman spectra for the $BaTiO_3$ sample before processing, after the two implantation steps, and after bonding and annealing. The final spectra match that of the sample before processing, indicating that proper postbond annealing can return the transferred layer to its original, single crystal state.

$BaTiO_3$ in this layer is significantly damaged due to large number of local defects, as well as large residual stresses. In previous work, the authors showed that the layer splitting mechanism induced a change in the hardness and Young's modulus of the implanted $BaTiO_3$ donor wafer.[28] This can be explained by an increase in strain near the bubble region during the layer exfoliation process. After postbond annealing, the micro-Raman curve is almost identical to the unprocessed, single crystal $BaTiO_3$. The sharp peaks at 272, 300, and 513.3 cm^{-1} are again present, and the smaller peak at 705 cm^{-1} has dissipated. These results verify that proper postbond annealing can return the transferred $BaTiO_3$ layer to its single crystal state.

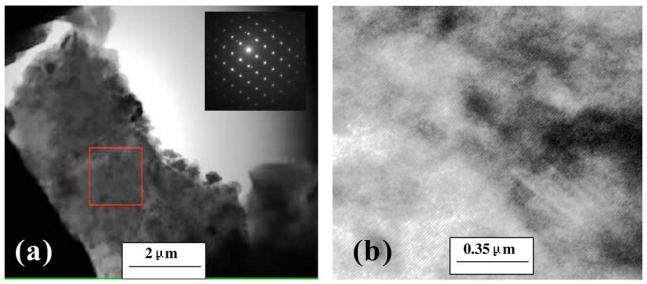

FIG. 6. (Color online) Transmission electron microscopy images of (a) low magnification with selected area diffraction pattern along the (112) zone axis shown as an inset, and (b) high resolution images.

Figure 6 shows transmission electron microscope images of $BaTiO_3$ bonded to an amorphous carbon coated Cu grid. High resolution images [Fig. 6(b)] show that the $BaTiO_3$ film has a single crystal lattice structure with a tetragonal lattice. This is confirmed by the selected area diffraction pattern shown as an inset in Fig. 6(a). Energy dispersive x-ray spectroscopy scans confirm that the $BaTiO_3$ thin film has a stoichiometric Ba:Ti:O ratio of 1:1:3. These results show that the composition of the transferred $BaTiO_3$ film is the same as the donor wafer, and the crystallinity of this layer can be recovered after bonding and subsequent annealing.

E. Domain characterization of transferred ferroelectric layer

Single crystal $BaTiO_3$ thin films with thicknesses between 150 and 800 nm were successfully transferred to Si_3N_4/Si and $Pt/Si_3N_4/Si$ substrates. The 800 nm thick films on $Pt/Si_3N_4/Si$ substrates were approximately 1×2 mm^2, and 400 nm thick films on Si_3N_4/Si were approximately 5×5 mm^2.[28] Atomic force microscopy line scans [Fig. 7(a)]

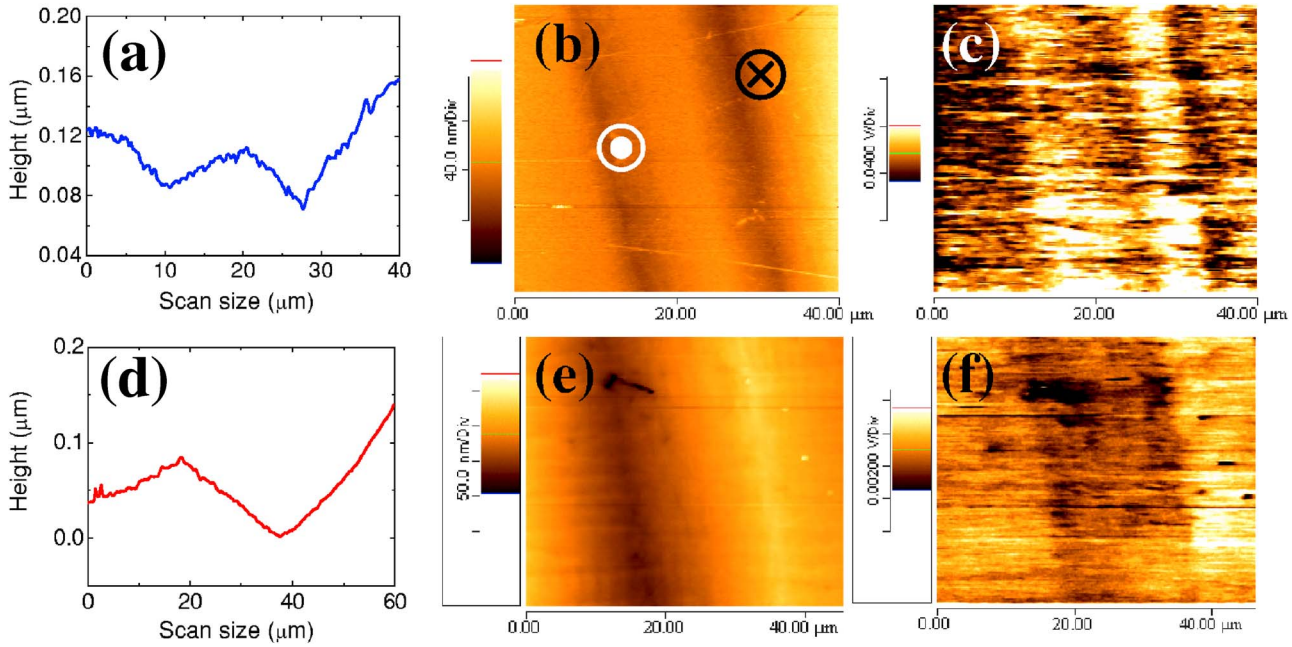

FIG. 7. (Color online) Comparison of surface morphology and polarization for bulk and transferred $BaTiO_3$. (a) AFM line scan of the transferred $BaTiO_3$ film along the domain walls, (b) AFM image of the transferred $BaTiO_3$ film, (c) PFM image of the transferred $BaTiO_3$ film, (d) AFM line scan of the bulk $BaTiO_3$ film along the domain walls, (e) AFM image of the bulk $BaTiO_3$ and (f) PFM image of the bulk $BaTiO_3$.

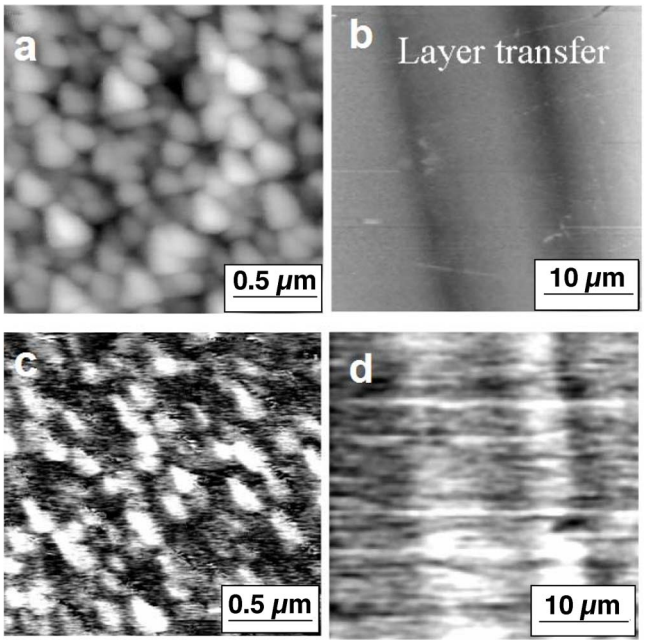

FIG. 8. (Color online) Comparison of AFM [(a) and (b)] and PFM [(c) and (d)] images for the $BaTiO_3$ thin films. (a) and (c) are of a PLD $BaTiO_3$ thin film. (b) and (d) are of a layer transferred thin film $BaTiO_3$. PFM measurement conditions were V_{ac}=1.5 V and a tip frequency of 20 kHz. Note that the AFM/PFM images of both films show different lateral scan sizes.

of the transferred $BaTiO_3$ samples show a domain structure similar to that of bulk $BaTiO_3$, Fig. 7(d). The *c*-*a* domain spacing in the transferred layer is approximately half of the equivalent distance in the bulk single crystal. This can be attributed to additional stresses which are imparted on the film during the layer transfer process. Piezoresponse force microscopy imaging in Fig. 7(b) also shows *c*-*a* domain configurations similar to a bulk single crystal, Fig. 7(e). The surface corrugation angle $[\theta=90°-2\arctan(a/c)]$ is 0.5°–0.6°. In the piezoresponse image [Figs. 7(c) and 7(f)], the bright and dark areas originate from regions where the polarization vectors point into and out of the plane, respectively. Since the domain structure is similar in both the single crystal and the transferred layer, one can conclude that the layer transfer yields high-quality films with properties very similar to bulk single crystals.

For comparison, a $BaTiO_3$ film grown using pulsed laser deposition is shown in Figs. 8(c) and 8(d). These films on Pt substrates produce crystallographically textured films which exhibit some grain misorientation. Their domain polarization characteristics and structure are influenced by domain misorientations and grain boundaries, Fig. 8(d). Therefore, pulse laser deposited $BaTiO_3$ films exhibit grain scale morphology as opposed to the domain scale morphology of the transferred films.

In order to confirm the piezoelectric nature of the $BaTiO_3$ film, we obtained a hysteresis curve [Fig. 9] for a single ferroelectric domain. Here the conducting atomic force microscope tip served as the top electrode. While both $BaTiO_3$ films showed piezoelectric hysteresis, the transferred film showed a larger piezoresponse, larger effective piezoelectric constant (d_{33}^{eff}) of 90 pm/V, and smaller coercive

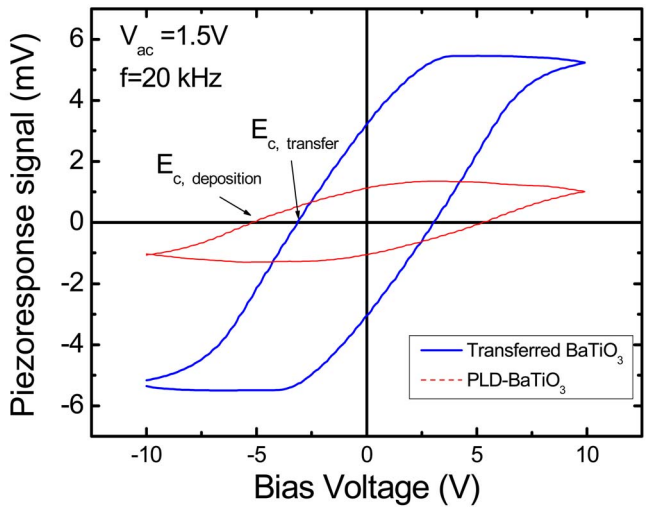

FIG. 9. (Color online) Local piezoresponse hysteresis curves comparing PLD $BaTiO_3$ on a Pt/Si substrate and layer transferred $BaTiO_3$ on Pt.

field (~20 kV/cm) than the donor substrate. Clamping effects are taken into account using the equation

$$d_{33}^{\text{eff}} = d_{33} - \frac{2d_{31}s_{13}}{s_{11}+s_{12}}.$$

The resulting single crystal d_{33} value (d_{33}=129 pm/V) is consistent with those reported elsewhere.[29–32]

IV. CONCLUSION

We have performed single crystal layer transfer and have reported mechanisms for cavity formation in ion-implanted, single crystal $BaTiO_3$. Analysis of the equilibrium concentration of species as a function of annealing temperature was performed. From this, it was shown that released hydrogen during thermal annealing suppresses the formation of volatile oxides which might otherwise degrade the performance of the ferroelectric films. The hydrogen pressure inside the platelets, created during thermal annealing, was sufficiently high to form cavities inside the implanted substrate. $BaTiO_3$ films, 150–800 nm thick, have been transferred onto Pt and Si_3N_4 layers. Micro-Raman analysis showed that the lattice damage of the $BaTiO_3$, which occurs during the layer transfer process, can be effectively removed with proper annealing. The transferred $BaTiO_3$ thin films show domains identical to those found in bulk crystals. Piezoresponse force microscopy shows that the film is piezoelectrically active with domain configurations similar to that of bulk crystals. The transferred films show larger piezoresponse and smaller coercive fields than those associated with $BaTiO_3$ films grown by traditional methods. Based on these results, ion implantation-induced layer transfer has been successfully utilized to create high-quality single crystal ferroelectric thin films that can be bonded to substrates with significant thermal expansion mismatch.

ACKNOWLEDGMENTS

This work has been supported by the Army Research Office (ARO-MURI) under Grant No. DAAD 19-01-1-0517

and the Center for Science and Engineering of Materials at Caltech, an NSF MRSEC Center. One of the authors (Y.-B.P.) wishes to acknowledge the support of the Postdoctoral Fellowship Program from Korea Science and Engineering Foundation (KOSEF) and Dr. I.D. Kim at MIT for PLD-$BaTiO_3$ sample preparation.

[1]J. F. Scott and C. A. Paz de Araujo, Science **264**, 1400 (1989).
[2]D. L. Polla and L. F. Francis, Annu. Rev. Mater. Sci. **28**, 563 (1998).
[3]Y. Xu, *Ferroelectric Materials and Their Applications* (Elsevier, New York, 1991).
[4]Q. Y. Tong and U. Gosele, *Semiconductor Wafer Bonding* (Wiley, New York, 1999).
[5]M. Bruel, Electron. Lett. **33**, 1201 (1995).
[6]K. Mitani and U. M. Gosele, Appl. Phys. A **A54**, 543 (1992).
[7]B. Aspar, H. Moriceau, F. Fournel, B. Aspar, B. Bataillou, A. Beaumont, C. Morales, A. M. Cartier, S. Pocas, C. Lagahe, E. Jalaguier, A. Soubie, B. Biasse, N. Sousbie, S. Sartori, J. F. Michaud, F. Letertre, O. Rayssac, I. Cayrefourcq, C. Richtarch, N. Daval, C. Aulentte, T. Akatsu, B. Osternaud, B. Ghyselen, and C. Mazuré, J. Electron. Mater. **30**, 834 (2001).
[8]Q. Y. Tong, K. Gutjahr, and U. Gosele, Appl. Phys. Lett. **70**, 1390 (1997).
[9]J. Zahler, C. Ahn, S. Zaghi, H. Atwater, C. Chu, and P. Iles, Thin Solid Films **403**, 558 (2002).
[10]M. Levy, R. M. Osgood, R. Liu, L. E. Cross, G. S. Cargill, A. Kumer, and H. Bakhru, Appl. Phys. Lett. **73**, 2293 (1998).
[11]T. Izuhara, I. Gheorma, R. M. Osgood, A. N. Roy, H. Bakhru, Y. M. Tesfu, and M. E. Reeves, Appl. Phys. Lett. **82**, 616 (2003).
[12]Y.-B. Park, J. L. Ruglovsky, and H. A. Atwater, Appl. Phys. Lett. **85**, 455 (2004).
[13]SOLGASMIX code with Chemsage, http://gttserv.lth.rwth-aachen.de
[14]G. E. Eriksson, Acta Chem. Scand. (1947-1973) **25**, 2651 (1971).
[15]SRIM 2003, http://www.srim.org/
[16]W. Han and J. Yu, J. Appl. Phys. **89**, 6551 (2001).
[17]R. A. Oriani, Annu. Rev. Mater. Sci. **8**, 327 (1978).
[18]Q. Y. Tong, K. Gutjahr, S. Hopfe, U. Gosele, and T. H. Lee, Appl. Phys. Lett. **70**, 1390 (1997).
[19]L. B. Freund, Appl. Phys. Lett. **70**, 3519 (1997).
[20]I. Szafraniak, I. Radu, R. Scholz, M. Alexe, and U. Gösele, Integr. Ferroelectr. **55**, 983 (2003).
[21]I. Radu, I. Szafraniak, R. Scholz, M. Alexe, and U. Gosele, Integr. Ferroelectr. **55**, 983 (2003).
[22]M. Weldon, V. Marsico, Y. Chabal, A. Agarwal, D. Eaglesham, J. Sapjeta, W. Brown, D. Jacobson, Y. Caudano, S. Christman, and E. Chaban, J. Vac. Sci. Technol. B **15**, 1065 (1997).
[23]M. Weldon, M. Collot, Y. Chabal, V. Venezia, A. Agarwal, T. E. Haynes, D. Eaglesham, S. Christman, and E. Chaban, Appl. Phys. Lett. **73**, 3721 (1998).
[24]C. Qian and B. Terreault, J. Appl. Phys. **90**, 5152 (2001).
[25]U. Gösele, Y. Bluhm, G. Kästner, P. Kopperschmidt, G. Kräuter, R. Scholz, A. Schumacher, St. Senz, Q.-Y. Tong, L.-J. Huang, Y.-L. Chao, and T. H. Lee, J. Vac. Sci. Technol. A **17**, 1145 (1999).
[26]S. Aggarwal, S. R. Perusse, C. W. Tipton, R. Ramesh, H. D. Drew, T. Venkatesan, D. B. Romero, V. B. Podobedov, and A. Weber, Appl. Phys. Lett. **73**, 1973 (1998).
[27]L. H. Robins, D. L. Kaiser, L. D. Rotter, P. K. Schenck, G. T. Stauf, and D. Rytz, J. Appl. Phys. **76**, 7487 (1994).
[28]Y.-B. Park, P. Nardi, X. Li, and H. A. Atwater, J. Appl. Phys. **97**, 074311 (2005).
[29]B. J. Rodriguez, Ph.D. Thesis, North Carolina State University, 2003.
[30]Parameters used in calculations: $d_{31}=-57.7$ pm/V, $s_{11}=8.3\times10^{-12}$ Pa^{-1}, $s_{12}=-2.7\times10^{-12}$ Pa^{-1}, and $s_{13}=-1.9\times10^{-12}$ Pa^{-1}.
[31]J. L. Ruglovsky, J. Li, K. Diest, K. Bhattacharya, and H. A. Atwater, Acta Mater. **54**, 3657 (2006).
[32]I.-D. Kim, Y. Avrahami, H. Tuller, Y.-B. Park, M. J. Dicken, and H. A. Atwater, Appl. Phys. Lett. **86**, 192907 (2005).